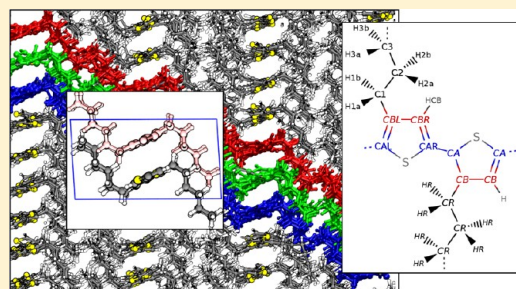


Effect of Polymorphism, Regioregularity and Paracrystallinity on Charge Transport in Poly(3-hexylthiophene) [P3HT] Nanofibers

Carl Poelking^{1,*} and Denis Andrienko^{1,*}¹Max Planck Institute for Polymer Research, Ackermannweg 10, 55128 Mainz, Germany

Supporting Information

ABSTRACT: We investigate the relationship between molecular order and charge-transport parameters of the crystalline conjugated polymer poly(3-hexylthiophene) (P3HT), with a particular emphasis on its different polymorphic structures and regioregularity. To this end, atomistic molecular dynamics is employed to study an irreversible transition of the metastable (form I') to the stable (form I) P3HT polymorph, caused by side-chain melting at around 350 K. The predicted side-chain and backbone–backbone arrangements in unit cells of these polymorphs are compared to the existing structural models, based on X-ray, electron diffraction, and solid-state NMR measurements. Molecular ordering is further characterized by the paracrystalline, dynamic, and static nematic order parameters. The temperature-induced changes of these parameters are linked to the dynamics and distributions of electronic coupling elements and site energies. The simulated hole mobilities are in excellent agreement with experimental values obtained for P3HT nanofibers. We demonstrate that a small concentration of defects in side-chain attachment (90% regioregular P3HT) leads to a significant (factor of 10) decrease in charge-carrier mobility. This reduction is due to an increase of the intermolecular part of the energetic disorder and can be traced back to the amplified fluctuations in backbone–backbone distances, i.e., paracrystallinity. Furthermore, by comparing to poly(bithiophene-*alt*-thienothiophene) (PBTTT) with its higher hole mobility, we illustrate how transport in P3HT is disorder limited as a result of its side-chain structure.



I. INTRODUCTION

Thiophene-based conjugated polymers have accompanied, if not originated the growing interest in conductive polymer materials and their application in organic field-effect transistors (OFETs) and organic photovoltaics (OPV).¹ By far the most studied representative of this class of materials is poly(3-hexylthiophene) (P3HT) with its regioregular (head-to-tail) isomer (see Figure 1a), as first synthesized by McCullough in 1992.²

While a rudimentary description of the thiophene compound itself can be found as early as 1883,³ the first polymerization reactions with high yield and small concentrations of impurities were reported only in 1980.^{4,5} The reason is the strong interaction of the conjugated backbones, rendering them essentially not processable, with up to 78% of the product being neither soluble nor meltable.¹ A more soluble derivative was desirable and, for this purpose, Elsenbaumer reported the synthesis of easily processable poly(alkylthiophenes) (PATs) in 1986.⁶ Solution-processed into thin films and doped, these materials could exhibit reasonable conductivities limited, however, by the disorder resulting from a regiorandom attachment of the side chains to the thiophene monomers.

It was the synthesis of regioregular (rr) P3ATs by McCullough in 1992 that had a fundamental impact on device performance and eventually paved the way for applications in OFETs and OPV cells. The very first OFET device with polythiophene as the semiconducting channel (1986) featured

field-effect mobilities of $10^{-5} \text{cm}^2/(\text{V s})$.⁷ Within ten years, mobility could be increased by three orders of magnitude by choosing rr-P3HT.⁸ PTs have also been tried in OLEDs, though less successfully because of their low photoluminescence quantum yield, i.e., high probability for nonradiative as compared to radiative recombination of electron–hole pairs.⁹ The first use of P3HT as a donor in an organic solar cell was, however, very much a success: With methanofullerene (PCBM) as an acceptor, the power conversion efficiency for the bulk-heterojunction was measured to be 4.4%, which back in 2005 was the highest-yet achieved efficiency in polymer-based solar cells.¹⁰

By 1993, the reason for the remarkable transport properties of rr-PATs was identified to be the exceptional supramolecular ordering and self-assembly properties of these polymer materials,^{11–13} which clearly distinguished rr-PATs from their regiorandom isomers. rr-PATs structures were not only found to be partially crystalline but also polymorphic with respect to backbone and side-chain ordering.¹⁴ In addition to regioregularity, a range of other factors has been shown to impact photophysical and transport properties, such as molecular weight, polymorphism, and polydispersity.^{15–18} Several shortcomings of rr-P3HT were also identified, most notably the high

Received: July 31, 2013

Revised: October 28, 2013

Published: November 8, 2013

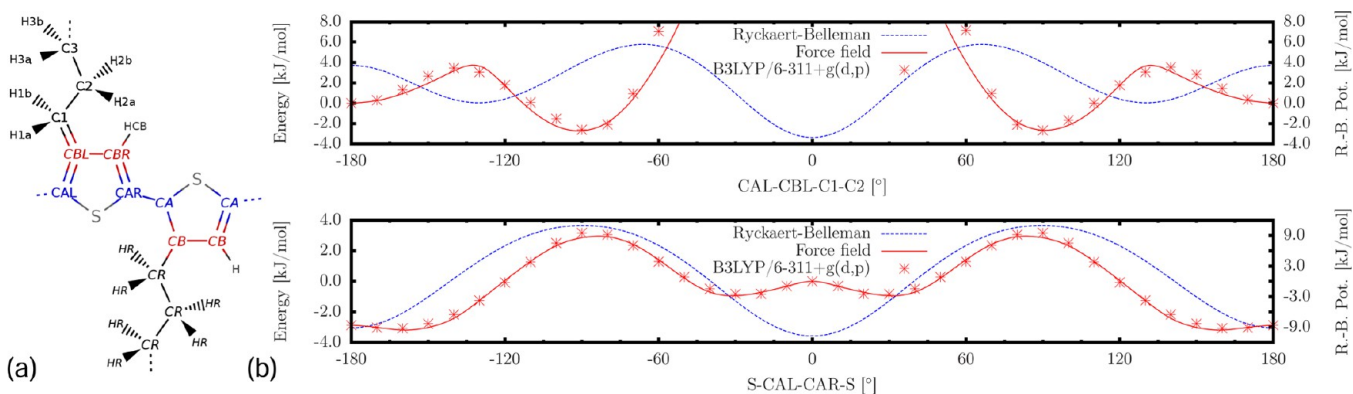


Figure 1. (a) Chemical structure of P3HT with atom names (left residue) and atom types (right residue) as used in the force field. (b) Force field and DFT scan for thiophene-hexyl (top) and thiophene–thiophene dihedral (bottom). Here $\pm 180^\circ$ corresponds to the trans, 0° to the cis conformation. Energies around 0° in the thiophene–hexyl scans peak at 45 kJ/mol, a result of steric repulsion between the C_β hydrogens and the sulfur of the adjacent repeat unit.

side-chain density. In P3HT it prevented side-chain interdigitation at ambient temperatures^{14,19,20} favoring more disordered (with respect to side chains and possibly backbone²¹) thermodynamic phases. The same high side-chain density promoted an additional σ -orbital density spill-out from the alkyl side chains into the delocalized π -system, resulting in a relatively high energy of the highest occupied molecular orbital and low ionization potential, deteriorating hole extraction in solar-cell devices as well as increasing susceptibility to oxidation.^{22,23} Finally, from the perspective of chemical synthesis, the noncentrosymmetric thiophene monomers limited the choice of polymerization techniques, with the risk of batch-to-batch variability.^{23,24} Pinpointed limitations inspired the synthesis of new materials, in particular hyperbranched thiophenes,^{25–27} donor–acceptor polymers,²⁸ and polymers with lower side-chain density,²⁹ with the prospect of improved device performance.

In spite of a certain saturation in the field, a fairly recent development is the fabrication of P3HT supramolecular self-assemblies, such as spherulitic structures³⁰ and crystalline nanofibers,^{31–33} which by now can be performed with excellent reproducibility, thanks to the current degree of control over the synthesis and processing of P3HT. These supramolecular structures offer, to some degree, a better control over chain ordering, and can hence facilitate improvement of OFET and OPV devices.¹³

Polythiophenes have been extensively studied using various simulation techniques, ranging from first-principles^{34,35} to atomistic^{36–38} and coarse-grained methods.^{39–41} At the force-field level of modeling, atomistic molecular dynamics simulations were carried out to characterize molecular ordering in pure amorphous (high-temperature) melts and pure crystalline domains of rr-P3HT.³⁶ The authors observed an onset of polymer self-assembly upon quenching the amorphous polymer melt to room temperature. Since all-atom MD simulations are not capable of modeling the formation of lamellar structures, more coarse-grained models were developed, e.g., by combining groups of atoms into superatoms interacting via (isotropic) potentials of mean force,³⁹ which, however, were not able to capture the anisotropy of π – π interactions. To remedy the situation, empirical soft-core potentials were introduced in ref 41 in order to model biaxial order in a nematic mesophase of a P3HT melt.

The crystalline molecular arrangement has also been linked to the density of states of P3HT,³⁵ demonstrating that the conjugation length is not sensitive to defects in side-chain attachment (degree of regioregularity), and implying that the mobility reduction is related to interchain transport. It has furthermore been shown for amorphous melts of P3HT that electrostatic energetic disorder has a stronger localizing effect than breaks in conjugation.⁴²

Establishing a link between morphology and charge transport properties in P3HT nanofibers is the main goal of our work. In particular, the focus will be on the effect of polymorphism and regioregularity on hole transport, i.e., the distribution and dynamics of site energies, electronic couplings, charge transfer rates, and, finally, the hole mobility. The paper is organized as follows. A summary of simulation techniques is provided in Methodology, section II. Crystalline phases of P3HT, as well as temperature-induced transitions between them are analyzed in section III, where several structural order parameters are introduced. With the help of these order parameters, the changes in the hole mobility are then linked to the changes in crystalline morphology in section IV. A brief summary is given in section V.

II. METHODOLOGY

A. Molecular Dynamics. To study the backbone and side-chain thermal fluctuations and ordering we employ molecular dynamics (MD) simulations. Here we will be dealing with highly ordered, crystalline to semicrystalline mesophases of P3HT and therefore time scales accessible to MD simulations (\sim microseconds) are long enough to adequately sample *local* chain ordering. At the same time, MD provides an atomic-scale morphology needed for the characterization of charge-transport parameters from first principles.

Since MD simulations rely on an appropriately parametrized functional form of the potential energy surface (PES), we first adapt the OPLS-AA^{43,44} force field by performing first principles calculations of a single chain (tetramer) PES in vacuum, in line with the earlier reparametrization of the thiophene–thiophene torsion potentials and partial charges on oligomers of P3ATs.³⁷ Particularly important are the dihedral potentials between thiophene units and between a thiophene unit and a partially conjugated side chain, potential energy surfaces of which are shown in Figure 1b. Figure 1a illustrates atom types as used in the definition of bonded potentials. The

force-field parameters for a number of bonded degrees of freedom and GROMACS input files for a single chain are available in the Supporting Information.

Starting configurations used in molecular dynamics simulations are prepared from preoptimized supercells that are themselves obtained from multiplication of unit cells adapted from experimental input after saturating the end groups with hydrogens (see section IIIA for details). Molecular dynamics simulations are performed in the NPT ensemble using the anisotropic Berendsen barostat⁴⁵ and a canonical velocity-rescaling thermostat⁴⁶ as implemented in the GROMACS simulation package.⁴⁷

All simulations are performed using chains of 20 thiophene units, formally corresponding to a molecular weight of 3.3 kDa. However, taking into account periodic boundary conditions as well as high crystallinity of the systems studied, our simulations mimic high molecular-weight P3HT. Structure optimizations using a steepest-descent method followed by a short stochastic dynamics run at low temperature with high friction constants are performed on $N_a \times N_b \times N_c = 5 \times 10 \times 20$ supercells, whereas larger, $10 \times 40 \times 20$, supercells are used for all MD runs. Here, N_a , N_b , N_c correspond to the number of lamellae, number of chains in the π -stack, and number of monomers per chain, respectively.

We investigate two different regioregularities of 100% (P3HT-100) and 90% (P3HT-90) regioleft P3HT. The disruption in the regioregularity is enforced on a per-chain basis: Starting from the P3HT-100 supercells, for each chain, two randomly picked regioleft thiophenes are converted into the regioright isomer by appropriately adapting bonded and nonbonded interactions as well as partial charges. This eventually leads to P3HT-90 morphologies where each chain is unique within the limit of random sampling. Initial atomic overlaps are removed using a steepest-descent method.

B. Charge Transport. The diabatic states⁴⁸ ϕ^i , ϕ^j of the charge-transfer complex are constructed from the highest occupied molecular orbital of an optimized (B3LYP functional, 6-311g(d,p) basis set) P3HT 20-mer. To account for the variation of dihedral angles along the polymer backbone, the orbitals are rotated into the respective coordinate frames of the thiophenes. The electronic coupling elements, $J_{ij} = \langle \phi^i | \hat{H}_{ij} | \phi^j \rangle$, with \hat{H}_{ij} the dimer Hamiltonian, are calculated for each molecular pair (ij) from the neighbor list using the semi-empirical ZINDO method.^{49–51} A pair of molecules is added to the list of neighbors if the distance between the centers-of-mass of any of the thiophene groups is below a cutoff of 0.5 nm. This small, fragment-based cutoff insures that only nearest neighbors are added to the neighbor list.

Assuming charge localization and nonadiabatic transport, the charge hopping rates can be computed using the high-temperature limit of the semiclassical Marcus charge-transfer theory⁵²

$$\omega_{ij} = \frac{J_{ij}^2}{\hbar} \sqrt{\frac{\pi}{\lambda_{ij} k_B T}} \exp \left[-\frac{(\Delta E_{ij} - \lambda_{ij})^2}{4\lambda_{ij} k_B T} \right] \quad (1)$$

where T denotes the temperature; J_{ij} , the electronic coupling element between molecules i and j ; $\Delta E_{ij} = E_i - E_j$, the site energy difference; and λ_{ij} , the reorganization energy. As such, the charge transfer rate, ω_{ij} , is very sensitive to the molecular alignment, or morphology. To some extent, J_{ij} depends only on the relative positions and orientations of molecules i and j ,⁵³ while the site energies E_i and E_j also include contributions due

to the local electric field created by the surrounding, i.e., they are functions of molecular positions and orientations within some volume around the pair.^{54,55} The potentials that give rise to site energies are calculated self-consistently using the Thole model,⁵⁶ reparametrized on the basis of the atomic polarizabilities and partial charges for a cation and a neutral molecule. For details, see the Supporting Information.

Reorganization energies λ_{ij} were evaluated via density functional theory (DFT) from the potential energy surfaces of a single molecule in a cationic and neutral state using the B3LYP functional and the 6-311+g(d,p) basis set. Since in a P3HT crystal the backbone is planar and large deviations from planarity are restrained by nonbonded interactions with neighboring chains, $\lambda_{\text{con}} = 0.103$ eV of a 20-mer was used to evaluate the rates.

Charge-carrier dynamics was modeled by solving the master equation for a charge carrier drift-diffusion in an applied electric field. All charge transport calculations were performed using the VOTCA package.⁵⁵

III. MORPHOLOGY

The supramolecular ordering in lamellar crystals is responsible for the remarkable charge-transport properties of P3HT. The crystalline packing has therefore been studied extensively²⁰ and from the early days on there have been indications that P3HT is polymorphic, i.e., adopts different crystalline structures depending on the solvent used, the annealing temperature, as well as the processing conditions. In 1992, Prosa et al. by means of X-ray diffraction proposed an “inverse-comb” molecular arrangement,⁵⁷ that is a lamellar structure of π -stacked thiophene backbones with alkyl side chains as spacers between adjacent stacks, and possible ordering of the side chains across the lamella–lamella interface. Even until now, the fine details of this structure could not be resolved entirely, with open questions concerning the tilt of the thiophene backbone as well as the packing and order of alkyl side chains.

The most prevalent structure of P3HT is the polymorph I, which is observed after annealing and therefore is the most relevant for organic electronics. It has a monoclinic unit-cell (for bulk P3HT samples XRD provides $a = 1.60$ nm, $b = 0.78$ nm, $c = 0.78$ nm⁵⁸). In 2010, an electron-diffraction study⁵⁹ proposed a tilted backbone orientation in a unit cell, in agreement with DFT-based calculations.⁶⁰

A polymorph II has been found to have a significantly smaller unit cell dimension along the a -axis and thus assumed to have interdigitated alkyl groups,^{14,61} which distinguishes it from form I. Upon heating, form II irreversibly transforms into form I. This phase transition is accompanied by a change in unit-cell dimensions, with interlayer spacings *increasing* and intrastack distances *decreasing*. A similar first-order phase transition has been described recently by a combined infrared-spectroscopy and wide-angle X-ray diffraction study²¹ for a noninterdigitated metastable polymorph that transforms into the stable form I, hence establishing a third polymorph I'.

A. Crystalline Packing and Polymorphism. In this work, we focus on the structure most relevant for organic electronics, i. e. P3HT with noninterdigitated side chains, polymorph I, as well as polymorph I', through which we have obtained the former. We first checked the stability of a proposed molecular arrangement in the monoclinic unit cell (form I⁵⁹) for a completely regioregular P3HT-100. This cell has a tilted backbone and side-chains oriented along the short diagonal of the a - b plane of the unit cell with an angle of 86.5° between the

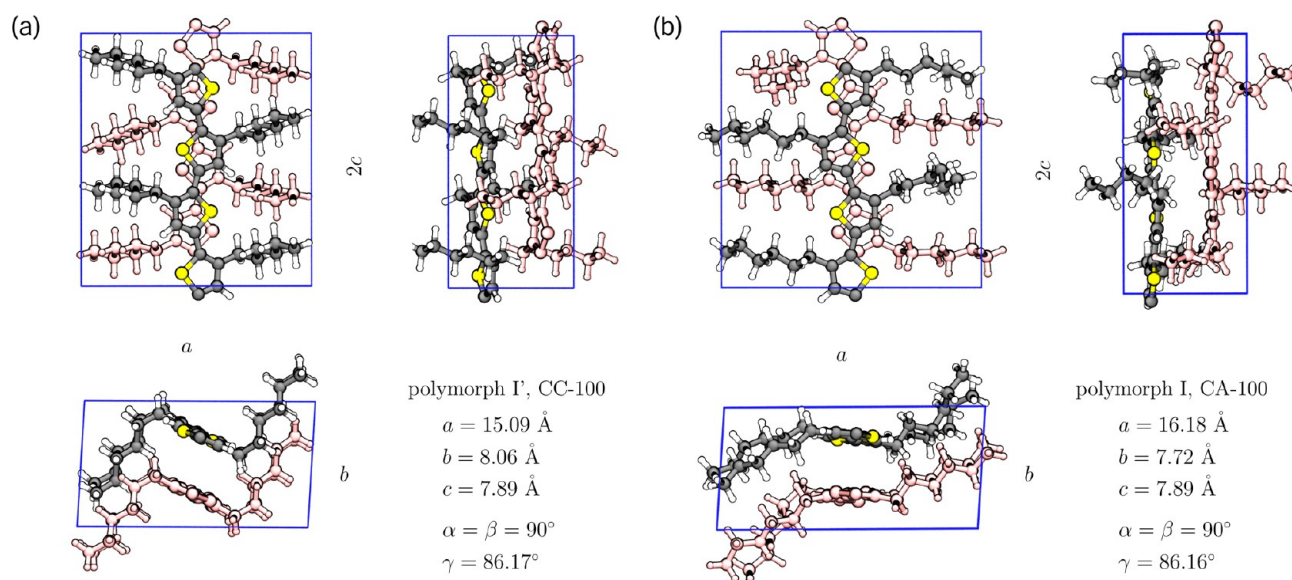


Figure 2. Regioregular poly(3-hexylthiophene) unit cells of polymorphs I' (a) and I (b) as obtained from molecular dynamics simulations after a steepest descent to the local energy minimum. Note the difference in backbone tilt from 25° (I') to 0°, measured with respect to the *a*-*c* plane.

a- and *b*-axis. The space group $P2_1c$ necessitates a crystal basis of at least two π -stacked dimers. The relative shift of these two dimers is not clearly specified, hence we set up unit cells with varying interlevel shifts. The structural model employed in this electron-diffraction study underestimates the carbon-carbon bond length in the hexyl side chains by about 0.1 Å. Correcting the distances to the OPLS-AA bond length of 1.529 Å requires rescaling of the *a*- and *b*-axis to avoid overlap of the alkyl chains of neighboring unit cells, which increases the dimensions of the unit cell to values somewhat larger than those reported in ref 59 (*a*, *b*, *c* \sim 1.6 nm, 0.78 nm, 0.78 nm). Moreover, these structures *flatten* entirely upon optimization such that the normals of the thiophene rings align with the *b*-axis and the hexyl side chains with the *a*-axis of the unit cell, leading to a significantly enlarged interlamellar spacing of more than 1.7 nm.

What eventually proved successful to obtain a tilted backbone was to (1) orient the hexyl chains along the long diagonal of the unit cell (this is the same as switching from $\gamma = 86.5^\circ$ to $\gamma = 93.5^\circ$) in order to create space for them to extend, (2) adjust the relative dimer shift to maximize the distance between the side-chains of the two dimers, (3) let the side chains relax to a low-energy conformation according to the PES in Figure 1b while constraining the backbone to the nontilted conformation, and (4) release both side chains and backbone. Hence, starting from a planar π -stack, the backbone can relax freely to its low-energy tilted conformation. The result of this optimization is shown in Figure 2a and the projections of the corresponding MD snapshot is shown in Figure 3a-c. As we will show later, this is the polymorph I' and not the thermodynamically favored polymorph I.

To study the phase transitions accessible to molecular dynamics, we simulate the obtained supercell at eight temperatures spaced 25K apart over the temperature range from 300 to 475 K, with the temperature raised linearly over a time interval of 1 ns and subsequent equilibration for 2 ns. We follow this procedure for both the high-regioregularity, P3HT-100, and medium-regioregularity, P3HT-90, case.

In order to introduce naming conventions for the studied morphologies, we mention already here that, upon heating, two

transitions can be observed, with the onset of the first one at around 350 K. We hence completed the heating cycle by cooling down both P3HT-100 and P3HT-90 from 425 K (i.e., well below the melting temperature) to room temperature, and subsequently performed a second heating cycle up to the melting regime. In what follows, we will show that the transition at low temperatures is related to melting of the side chains, and therefore refer to the systems that underwent the heating *and* cooling cycle as CA-100 and CA-90 as opposed to CC-100 and CC-90, in order to highlight that the backbone is crystalline (C) even in the samples that were subjected to the full cycle, whereas side chains have entered a more disordered, amorphous (A) state. We thus study the temperature behavior of *four* systems that differ with respect to regioregularity (90% and 100%) and crystallinity of side chains (CC and CA). Unit cells and MD snapshots of the regioregular systems, CC-100 and CA-100, are shown in Figure 2 and Figure 3, respectively.

We will now investigate more closely how the temperature behavior, in particular the phase transition at around 350 K, is reflected in unit cell dimensions and dynamic, static, and paracrystalline order parameters for the side-chain and backbone structure.

B. Unit Cell. Figure 4a,b summarizes the temperature behavior of the *a* and *b* vectors for all four systems. Note that *a* is related to the interlamellar spacing and *b* to twice the π -stacking distance as well as the backbone tilt angle. The *c* vector of the unit cell remains unchanged, since it is oriented along the covalently bonded backbone. By comparing CC-100 and CA-100 at 300 K it becomes obvious that the *a* vector (Figure 4a) *increases* in magnitude by roughly 0.1 nm, whereas the *b*/2 distance *decreases* from 0.40 to 0.38 nm. Note that the same changes in unit-cell dimensions have been detected experimentally by means of X-ray diffraction for the transition from form II to form I¹⁴ for P3ATs as well as from the recently proposed form I' to form I²¹ for P3HT.

The expansion along the *a* axis can be easily understood for both phase transitions: In the former case, side chains change from an interdigitated to noninterdigitated configuration,²⁰ whereas in the second case, as can be seen in Figure 2, the expansion is largely due to the more extended side chains.

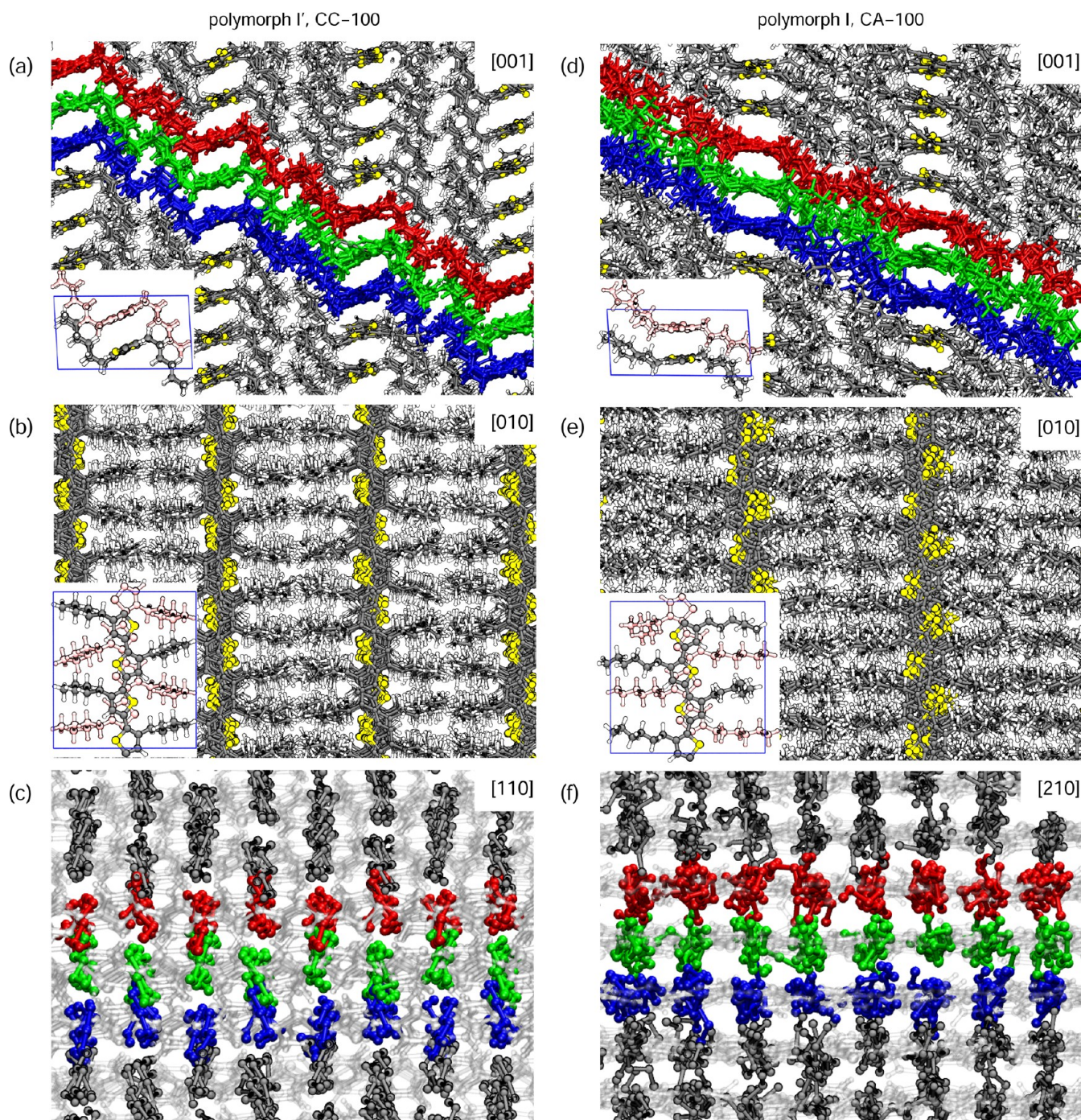


Figure 3. Regioregular poly(3-hexylthiophene) lamellar crystals of polymorphs I' (a–c) and I (d–f) as obtained from molecular dynamics simulations. Projections are constructed along the (a, d) [001], (b, e) [010], (c) [110], and (f) [210] crystal direction. Note the degree of interlamellar correlation mediated by the hexyl side chains even in their disordered phase.

Furthermore, in CA-100, the backbones are no longer tilted with respect to the a - c plane. This is clearly reflected in the contraction of the unit cell along the b axis. Note that this is *not* related to shorter π - π distances: Even though the b vector decreases in size, the distance of the planes that incorporate the backbones *increases* from 0.36 to 0.38 nm. The putative decrease is hence due to the interplay of (1) the tilted to nontilted transition, (2) the slightly staggered configuration of the backbones in CC-100 and CC-90, and (3) the monoclinic angle of 86.5° , which interestingly remains the same for all configurations.

The π -stacking distance of 0.38 nm matches well with what is reported in literature for the stable polymorph I, for example by a combined X-ray diffraction and solid-state NMR study.⁶² Indeed, contrary to results from earlier theoretical and experimental studies,^{34,59} this recent study suggested a nontilted structure for polymorph I, as we find for CA-100 and CA-90. Furthermore, the nature of their structural model with respect to the tilting of the side chains appears to agree well with what we find for these two systems in our simulations. Considering additionally the temperature stability of CA-100

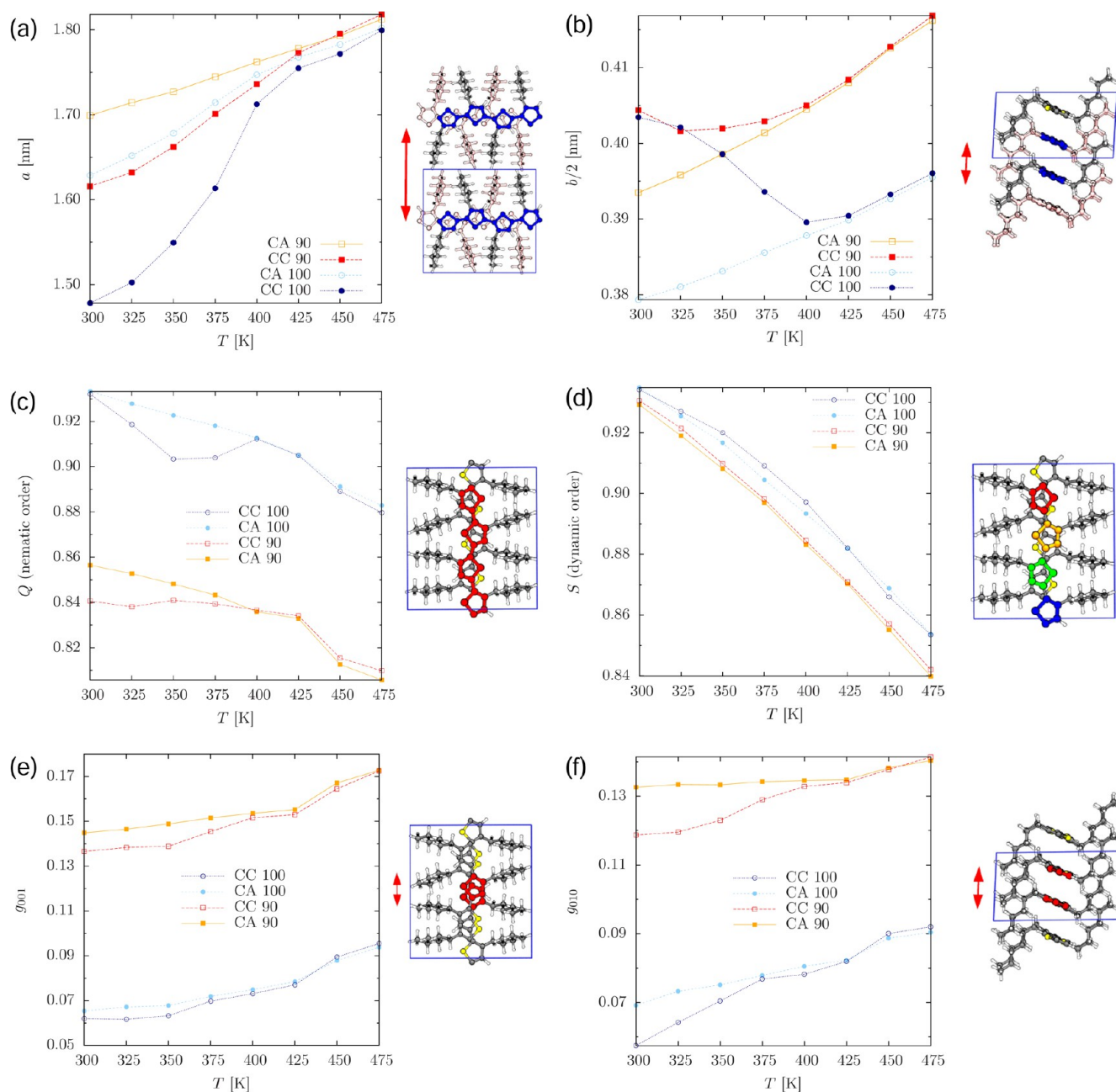


Figure 4. (a, b) Unit-cell changes upon heating over the temperature range from 300 to 475 K reflecting the interlamellar spacing (a) and stacking distance (b). Note that the actual π -stacking distance increases in spite of the decrease in $b/2$. (c, d) Dynamic and nematic parameters of the thiophene normal over the temperature range from 300 to 475 K. (e, f) Paracrystallinity measured along the c and b axes. Note the 2-fold increase in g in the materials with reduced regioregularity. The transition from form I' to form I can be seen best from the changes in unit-cell dimensions as shown in parts a and b. The onset of melting is reflected in the nematic order (part c). Since we are dealing with small system sizes, transitions are broad and transition temperatures can only be qualitatively assigned.

and CA-90 up to the melting regime, we identify the CA form as P3HT polymorph I.

Further consistency is achieved in terms of the b -vector contraction as also observed experimentally for the II-to-I phase transition, investigated for P3ATs,¹⁴ and the I'-I phase transition investigated for P3HT.²¹ In either case, b decreases. Specifically, for P3HT form II, $b/2 = 0.44$ nm has been reported,⁶³ combined with an exceptionally short interlamellar distance of only 1.18 nm. This very small magnitude of the a -vector is most likely due to interdigitated side chains and a strongly tilted backbone. The latter should hence account for the large $b/2$, which is not due to increased π - π distances, but

simply the staggered stacking with a sizable tilt angle. In simulations, the tilt angle of CC-100 amounts to roughly 25° , and is accompanied by a $b/2 = 0.40$ nm. For form II, one would hence expect a tilt considerably larger than these 25° . Irrespective of the value for the tilt angle, the apparent decrease in $b/2$ upon heating should be related to a planarized backbone, indicating that both forms I' and II have tilted backbones, with the tilt measured against the a - c plane. We hence identify our system CC-100 with the polymorph I'.

It should also be pointed out that CC-100 features interesting similarities with the structural model proposed for epitaxial thin films of regioregular P3HT.⁵⁹ This electron-

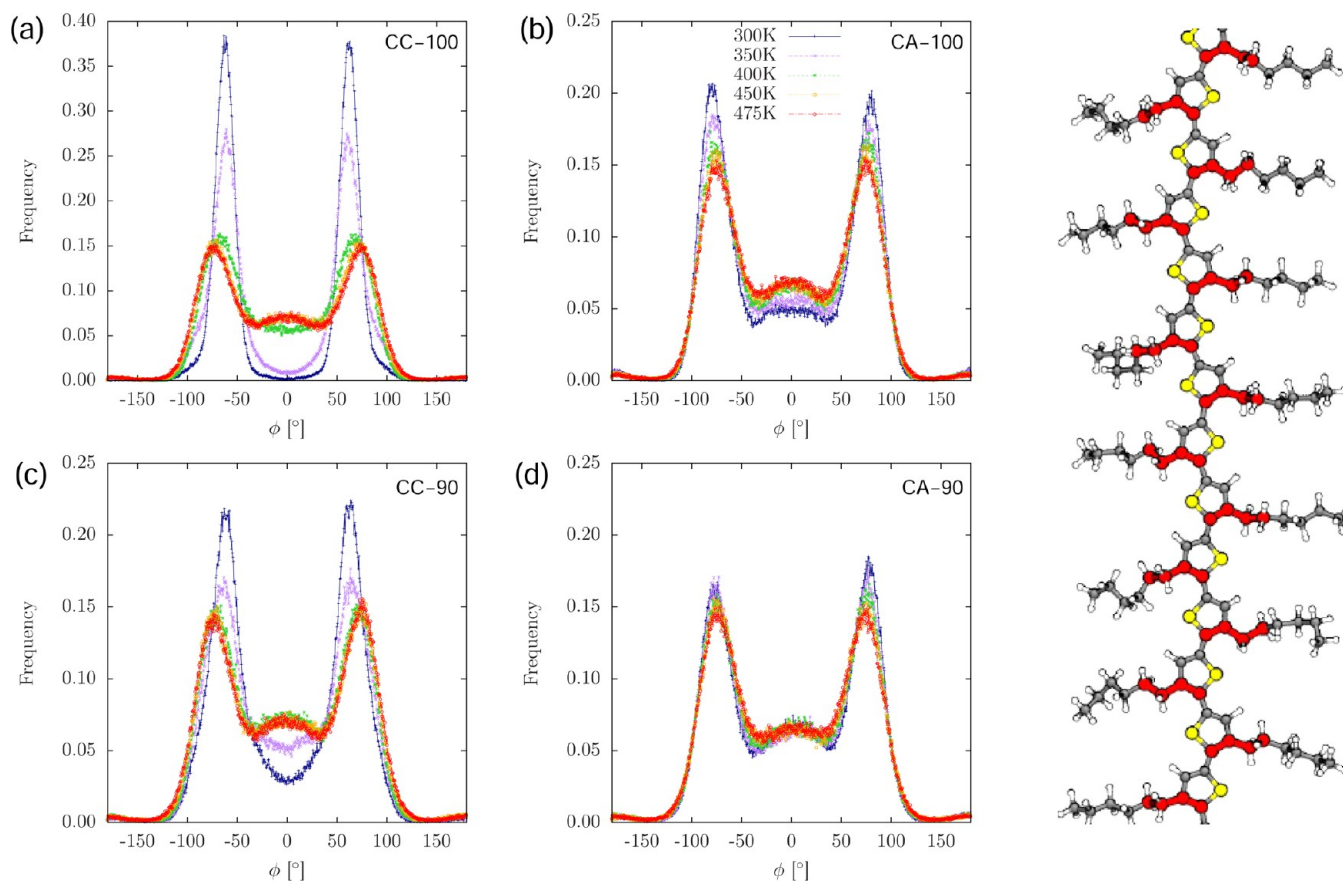


Figure 5. Change in the distribution of dihedral angles ϕ (CAL/R-CBL/R-C1-C2) over the temperature range from 300 to 475 K in intervals of 50 K. $\phi = 0^\circ$ corresponds to the *trans*, and $\pm 180^\circ$ to the *cis* conformation. Note how the structural transitions from CC-100 to CA-100 and CC-90 to CA-90 are accompanied by a population increase in *trans* conformers.

diffraction study is conceived to describe P3HT form I,²⁰ however, both the numerical value for the backbone tilt as well as the proposal of an (orthogonal) subcell for the crystallized side chains, which becomes visible upon projection along the [120] direction, go in line with our findings. Indeed, a previous study has expressed doubts about to which degree the structural model of ref 59 is applicable to the thermodynamically stable polymorph.⁶² Also, the form I' has been observed for P3HT crystallized by means of an extremely slow evaporation rate of the solvent at slightly lower than room temperature. It is hence plausible that both epitaxy and slow evaporation rates favor the crystallization into form I'.

To summarize, analysis of the unit-cell dimensions allowed us to identify the (irreversible) transition from P3HT polymorph I' to I upon heating. This transition is characterized by a reorganization of both side chains and conjugated backbone: The interlamellar spacing increases, while the transition from a tilted to nontilted backbone leads to a putative decrease in the *b* (π -stacking) vector, which effectively translates into an increase in backbone–backbone distances. We will now study in more detail static and dynamic properties of backbones and side chains upon this transition.

C. Side-Chain Conformations. In terms of side-chain structure, one of the key determinants is the configuration of the partially conjugated dihedral that connects the hexyl groups to the thiophene units. Distributions for this dihedral angle are shown in Figure 5. At low temperatures, systems CC-100 and CC-90 (Figure 5a,c respectively) are well ordered in the sense that it is mostly the single-chain potential minimum around 90°

that is populated (compare to the PES in Figure 1, but take into account the different convention used with 0° indicating the *cis* and $\pm 180^\circ$ the *trans* state). Note that the maximum of the population is shifted away from the single-chain PES minimum toward the *trans* conformation by ca. 30° due to the effects of crystal packing. For CC-100, there is an abrupt increase in the fraction of hexyl groups that adopt a *trans* configuration upon heating above 350 K. The same change is observed for CC-90. However, due to the 10% regio-right isomers mixed into an otherwise regio-left system, defects are introduced, such that already at room temperature a certain fraction of dihedrals populates the potential minimum that is associated with *trans* conformers. For systems CA-100 and CA-90 (Figures 5b,d respectively), the abrupt increase in *trans* conformers upon heating is not observed. A large fraction of *trans* conformers is hence characteristic of polymorph I, whereas side chains in form I' tend to localize in the single-chain PES minimum. This is in qualitative agreement with solid-state NMR results that suggest weak coupling between the C_4 atom CBR of the five-ring and the C_α hydrogens H1a and H1b (see Figure 1 for reference).⁶² This is the case when these hydrogens are twisted as far as possible away from the thiophene unit, which can only be realized by arresting the CAL–CBL–C1–C2 dihedral in a *trans*-type conformation.

D. Side-Chain Mobility. In the previous section, we have addressed the temperature- and regio-regularity-induced changes in dihedral-angle populations. Here we investigate whether the structural transition mirrored by these populations is accompanied by a change in side-chain mobility. To this end,

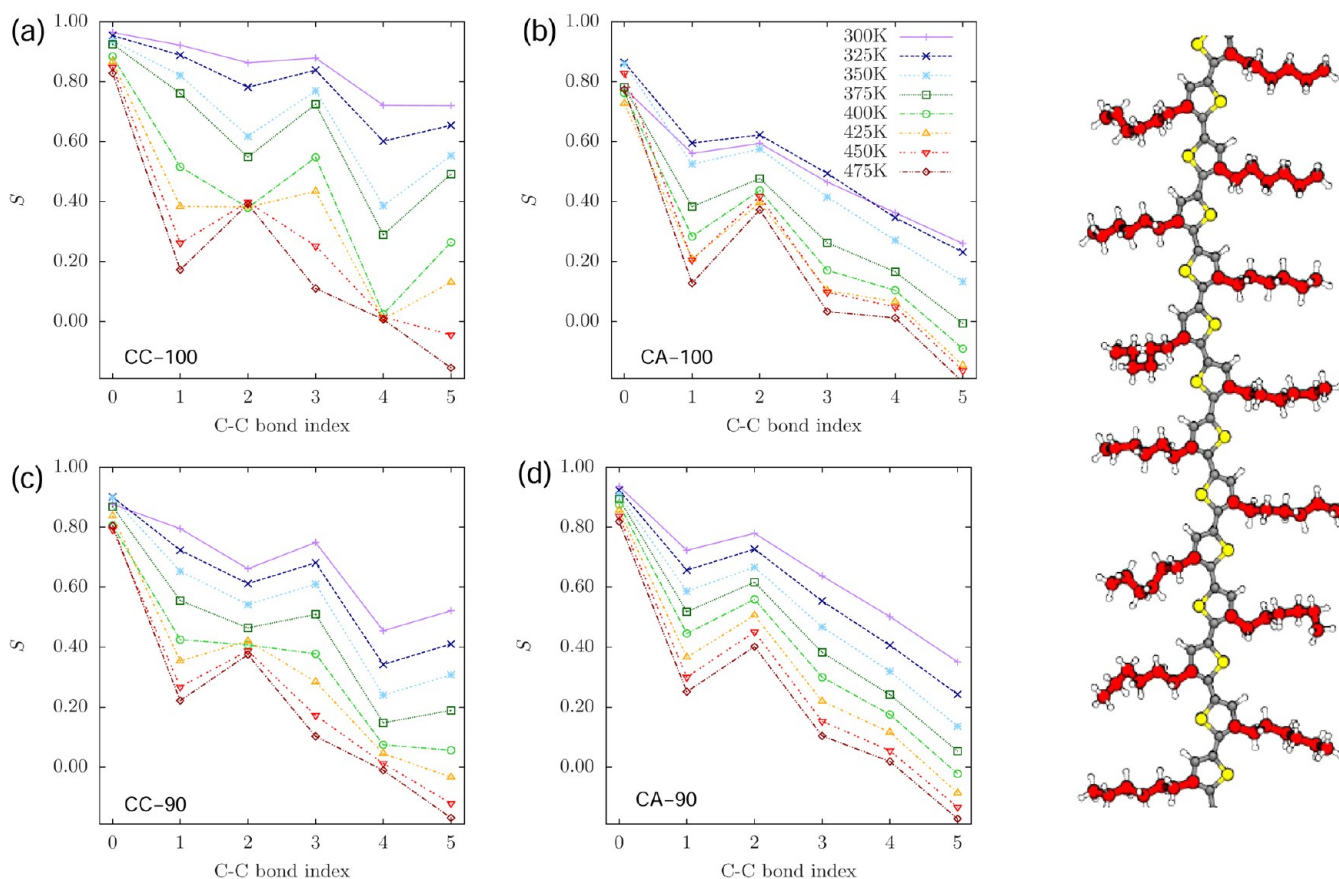


Figure 6. Decrease in dynamic order of side chains, estimated from the dynamic order parameter of successive carbon–carbon bonds in the hexyl group while heated over the temperature range from 300 K (purple) to 475 K (brown) in intervals of 25 K. Bond index 0 labels the C_3 – C_α bond, index 1 labels the C_α – C_β bond, and so forth.

we calculate the dynamic order parameters associated with the hexyl bonds, which can also be extracted from solid-state NMR measurements^{64–67}

$$S = \left\langle \frac{1}{N} \sum_{i=1}^N \left(\frac{3}{2} (\vec{M}^{(i)} \cdot \vec{m}^{(i)})^2 - \frac{1}{2} \right) \right\rangle \quad (2)$$

where $\vec{M}^{(i)} = \langle \vec{m}^{(i)} \rangle$, $\langle \dots \rangle$ denotes time averaging, N is the number of molecules in the system, $\vec{m}^{(i)}$ is the instantaneous vector of interest (e.g., the bond vector of neighboring carbons in the case of alkyl side chains). $S = 1$ implies a constant in time for the bond orientation, while $S < 1$ indicates that the orientation is changing over time. Figure 6a–d illustrates the temperature behavior of the hexyl side chains, where the carbon–carbon bonds are used as vectors \vec{m} and indexed according to their distance from the C_3 – C_α bond. With CC-100 (Figure 6a), the side chains are initially in a highly crystalline state. Upon increasing the temperature, two melting transitions can be observed. We can link the low-temperature transition around 350 K to the I' – I phase transition, and the second high-temperature transition beyond 425 K to the melting regime of the backbone. Note that the system CA-100 undergoes additional side-chain melting as of 375 K, which is reflected in a larger-than-linear decay in side-chain mobility.

Side-chain reordering in P3HT has been linked experimentally to crystal–crystal phase transitions both for the I' – I ²¹ and II – I transitions.¹⁴ In ref 21, increased disorder in side chains was evidenced by band shifting in infrared spectra when going from I' to I . The authors find hexyl groups to be

significantly more ordered in the low-temperature polymorph I' . Specifically, the packing of the terminating methyl groups is reported to get more disordered when switching to the thermodynamically stable polymorph. Our simulations suggest the same trend, with the dynamic order parameter for the methyl group decreasing from $S = 0.80$ in CC-100 at 300 K to a value of $S = 0.40$ calculated for CA-100 at the same temperature. A value of $S = 0.80$ for the terminating carbon–carbon bond is perhaps surprising since the paradigm of crystalline side-chain domains in regioregular/regiorandom P3HT is somewhat more recent.^{58,68,69} Side-chain melting has also been studied by ^{13}C solid-state NMR in relation with the II – I phase transition¹⁹ (note that the authors use interchanged labels II and I , opposite to the convention in this work). Comparing with our simulations, however, it seems possible that the authors investigated the side-chain melting transition that we observe in CA-100 (i.e., form I'), since the backbone is reportedly unaffected and disordering in the side chain appears rather subtle. Indeed, dynamic order parameters for CA-100 from simulations match within ± 0.1 what is measured there.

For the systems of medium regioregularity, CC-90 and CA-90, the qualitative picture remains the same. At low temperatures the side chains in CC-90 are more mobile than in CC-100, converging to similar values upon increasing temperature. This is expected since at high temperatures side chains are in an entirely disordered state and defects in side-chain attachment no longer have an impact on chain dynamics. At low temperatures, however, the increased disorder makes

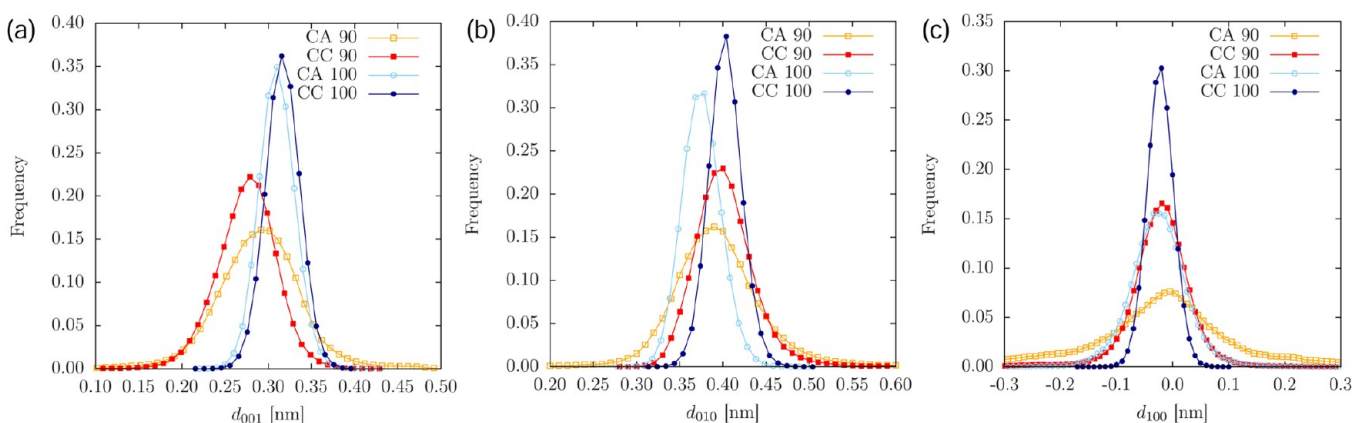


Figure 7. Distribution of distances between successive monomers of neighboring chains for two polymorphs, each with high and medium regioregularity along the (a) [001], (b) [010], and (c) [100] crystal direction. Note the high concentration of slipping-type defects caused by regioregularity defects in CA-90, graph c.

the I' to I transition less pronounced for CC-90 compared to CC-100. In fact, for CA-90, the temperature behavior is almost linear, with virtually no side-chain melting taking place as was observed for CA-100. Interestingly, at low temperatures, side chains in CA-90 are less mobile than in CA-100, which is due to the glassy state induced by the defects in regioregularity.

As a final aspect of side-chain ordering, we will comment on the degree of interlamellar ordering, as has been investigated experimentally.^{19,57,58} It is interesting to note that in spite of the absence of side-chain interdigitation between chains of neighboring lamellae, simulations suggest considerable inter-layer ordering for CA-100, i.e., form I, as is indicated in Figure 3. With increased disorder in side chains, this positional correlation decays. Indeed, for CA-90, over the time of the MD simulations, lamellae underwent a slow undirected gliding motion alongside each other. Whether side-chain melting by itself promotes this decorrelation, as suggested in ref 58, we cannot state with certainty due to the short time scales accessible via MD.

E. Backbone Ordering. So far we have limited the discussion to structural rearrangements of alkyl side-chains. For charge transport, however, the backbone packing and dynamics is more important. In this section we will characterize the dynamics and ordering of polythiophene backbones. To this end, we use three types of order parameters: dynamic (as already employed for the side chains), nematic and paracrystalline.

First, the *orientational* ordering of the conjugated subunits in the polymer backbone is assessed by the nematic order parameter Q ,⁷⁰ i.e., the largest eigenvalue of the nematic order parameter tensor, \hat{Q}

$$Q_{\alpha\beta} = \left\langle \frac{1}{N} \sum_{i=1}^N \left(\frac{3}{2} u_{\alpha}^{(i)} u_{\beta}^{(i)} - \frac{1}{2} \delta_{\alpha\beta} \right) \right\rangle \quad (3)$$

Here N is the number of conjugated subunits (thiophene rings) and $\vec{u}^{(i)}$ denotes a vector perpendicular to the conjugated planes of these units. $Q = 1$ implies perfect alignment of the unit vectors \vec{u} and $Q = 0$ corresponds to an isotropic angular distribution of these vectors. This should be contrasted with the dynamic order parameter S , which does not correlate unit vectors \vec{u} among each other, but rather a vector \vec{u} against its time average. Hence, for an amorphous glass at zero temperature $Q = 0$, whereas $S = 1$.

Nematic and dynamic order parameters for the thiophene normal vector as a function of temperature are shown in Figure 4, parts c and d, respectively. For all four systems, S exhibits a linear decrease with temperature. This is in agreement with ref 19, where the authors found that disordering of the side chains does not affect backbone dynamics, with the associated NMR order parameter as high as $S(\text{C4-H}) = 0.92$, in good agreement with what we find at 300 K for CA-100. Defects in the regioregularity lead to a slightly enhanced mobility of the backbone, with a constant offset from the regioregular case as small as 0.01.

The effect of defects in regioregularity on the static order, Q , shown in Figure 4c, is very different. First, an offset of ca. 0.08 separates CC-100/CA-100 from CC-90/CA-90, indicating that a significant amount of static disorder is introduced in less regioregular systems. Furthermore, the phase transition from I' to I clearly shows in the temperature behavior of Q , and, surprisingly, the *decreased* order in the side chains is in this case accompanied by *increased* nematic order. This can only be rationalized in terms of the backbone rearrangement, which changes from tilted over to nontilted. At higher temperatures (425 K) the onset of the backbone melting manifests itself as an abrupt decrease in nematic order.

F. Backbone Paracrystallinity. Finally, to quantify the degree of *positional* disorder of the conjugated subunits along specific crystal directions, the paracrystallinity parameter g_{hkl} is evaluated as

$$g_{hkl}^2 = \frac{\langle d_{hkl}^2 \rangle - \langle d_{hkl} \rangle^2}{\langle d_{hkl} \rangle^2} \quad (4)$$

where d_{hkl} is the distance between the centers of mass of two closest conjugated subunits, projected on the $[hkl]$ -direction. We calculate g_{hkl} for two crystal directions, [010] corresponding to the π -stacking direction, and [001] corresponding to the long axis of the polymer chains. The temperature dependence of g_{001} and g_{010} is given in Figure 4, parts e and f, respectively. As for the nematic order parameter, both the I'-to-I and melting transition appear in the temperature characteristics of CC-100 and CC-90, with systems CA-100 and CA-90 featuring an otherwise linear temperature dependence in g_{001} and g_{010} . It is striking, however, how a reduction in regioregularity by 10% leads to a twofold increase in paracrystallinity. For instance, comparing CA-100 to CA-90 at 300 K, g_{001} increases from 7% to 14%. As a qualitative measure, highly crystalline materials

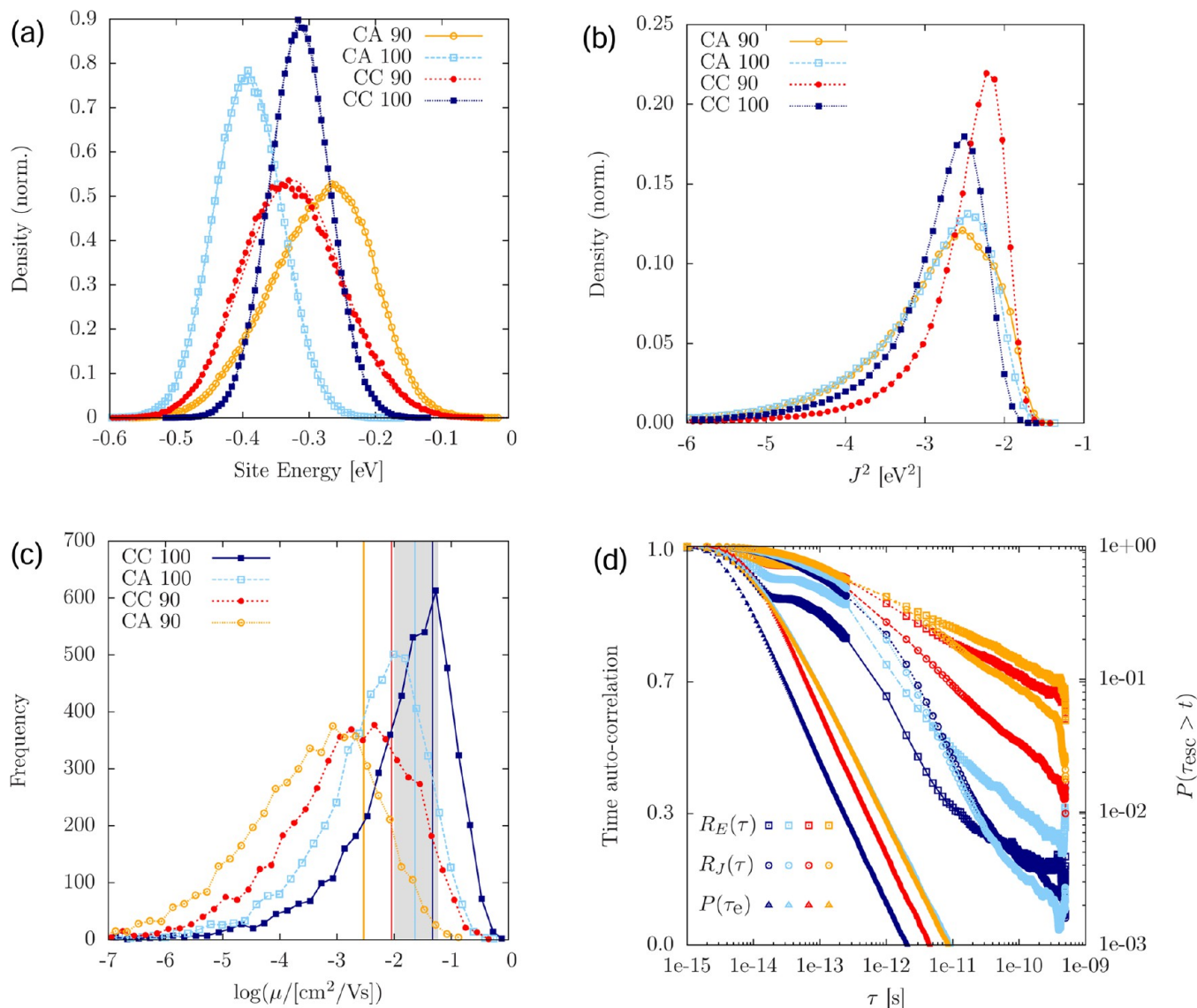


Figure 8. (a) Densities of state together with Gaussians fitted to CC-100, CA-100, CC-90. Note the aberration from a Gaussian line shape found for CA-90, which results from slipping defects in the lamellar stack. (b) Distributions of squared electronic couplings. (c) Distribution of lamellar mobilities. Vertical lines indicate averages. The gray bar includes the range of mobilities measured in P3HT nanofibers.^{32,73,74} (d) Autocorrelation functions for site energies (squares) and transfer integrals (circles) compared to the tail distribution of escape times (triangles). Color coding conforms to graphs a–c.

feature g 's of less than 1%. A g value between 1% and 10% is associated with paracrystalline materials. $g > 10\%$ is indicative of melt-like systems.⁷¹ Thus, paracrystallinity is a convenient order parameter when one needs to distinguish between the degree of side-chain regioregularity, as it is very sensitive to the defects in side-chain attachment.

It is instructive to also study the distributions of the d_{hkl} that are related to the paracrystallinity parameters. Parts a–c of Figure 7 depict distributions for all three principal axes of the lamellar crystals, [001], [010], and [100], respectively. Again, it is obvious, for all three crystal axes, how defects in the regioregularity lead to considerable broadening of the distributions. This is most prominent for the distributions for d_{100} , where [100] is the crystal direction associated with the slipping motion of the backbones *perpendicular* to the long axis of the polymer chains. Additionally, it is not only the width of the distributions that changes, but also their mean. For instance, the systems CA-90 and CC-90 feature systematically smaller

interchain shifts. Finally, the coplanar stacking in CA-90 in combination with the defects in regioregularity leads to a non-Gaussian shape of the distribution of projected distances, with a long tail of monomer–monomer distances hinting at sizable defects in the interchain packing.

Having now discussed in great detail not only the structural impact of defects in side-chain attachment, but also morphological changes that accompany the phase transition from form I' to form I, we finally comment on the driving force that causes this structural transition. We recall that the interlamellar spacing increases, as does the effective π -stacking distance. This implies a smaller density for the thermodynamically stable polymorph I compared to I', which is somewhat unexpected for the class of van-der-Waals-bound solids, where a *less* dense packing usually entails *reduced* stability. Furthermore, the backbones leave their energetically favored tilted stacking mode. Consequently, the existence of the phase transition and irreversibility thereof have to be linked to the larger excluded

volume of the more mobile, i.e., less ordered side chains: Form I is stabilized by the associated increase in entropy. This refers back to the large side-chain number density, which is significantly higher than for other hairy-rod semicrystalline polymers such as PBTBT, where the side-chain melting transition is reversible.⁷² Notably, it is the increase in excluded volume of the side chains that is capable of straightening out the backbone.

In what follows, we will investigate how these structural properties and changes can be related to transport parameters.

IV. CHARGE TRANSPORT

With the molecular dynamics trajectories at hand, we now evaluate the energetic landscape and electronic coupling elements for hole transport.

A. Energetic Disorder. In crystalline morphologies considered here, P3HT backbones are fully conjugated and a charge delocalizes over an entire oligomer. Hence, the conjugated segment length is 20 thiophene units, the internal contribution to the ionization potential does not change from segment to segment and the energetic disorder is mostly due to a locally varying electrostatic potential.

The distributions in hole site energies, i.e., the differences between the energies of the system when a selected molecule is in the cationic or neutral state excluding the constant internal contribution related to the gas-phase ionization potential, are shown in Figure 8a, together with the fits to a Gaussian function,

$$f(E; \langle E \rangle, \sigma^2) = \frac{1}{\sqrt{2\pi}\sigma} \exp\left[-\frac{1}{2}\left(\frac{E - \langle E \rangle}{\sigma}\right)^2\right] \quad (5)$$

As one can see, both the width σ and the mean $\langle E \rangle$ of the distribution depend on the side chain packing and polymer regioregularity. As expected, 100% regioregular P3HT always has narrower site-energy distributions than the 90% P3HT. Interestingly, the hole becomes less stable upon side-chain melting in the 100% regioregular P3HT (the distribution shifts to more negative numbers by 0.1 eV), while it is stabilized upon side-chain melting in the 90% regioregular P3HT. Note that the shift of the mean of the distribution is not essential for a one-component system, since only site-energy differences enter in the Marcus rate expression, eq 1, but can play a role in a bulk-heterojunction solar cell, where a relative level alignment of a donor and acceptor are important.

We can attribute specific structural modes to the changes in the energetic DOS. We observe how the width in the distributions appears to be governed by regioregularity, with CC-100 and CA-100 having virtually identical widths of $\sigma = 45$ and 51 meV, whereas CC-90, CA-90 are energetically more disordered with $\sigma = 74$ and 75 meV, respectively. The magnitude of the disorder compares well with the width of the DOS as extracted from time-of-flight experiments,^{12,17} where values for σ of 56 and 71 meV, respectively, have been proposed from a fit of the field-dependence of the mobility as obtained within the Gaussian Disorder Model.⁷⁶ In ref 12, σ 's did not vary significantly between 94% and 98% regioregular P3HT, but it is not immediately clear, how sensitive the fitting procedure is to deviations of only 30 meV, a difference in energetic disorder that may however be critical in the case of low-dimensional transport, as evidenced in what follows.

In order to relate the broadening of the DOS to a structural mode, we consider again Figures 4c–f and 7. There is a

regioregularity effect observable for all paracrystallinity parameters as well as the nematic order parameter calculated for the backbone. The decrease in nematic order is moderate with a relative reduction in Q of only 7%. We need to account, however, for an increase in energetic disorder by a factor 1.7, and therefore turn to paracrystallinity instead: Since the interaction between charged conjugated backbones is seminal here, we link the increase in energetic disorder to g_{010} , i.e., paracrystallinity along the π -stacking direction, which increases by approximately the same factor 1.7. Considering that the hole-quadrupole interactions associated with thiophene dimers is the leading contribution to site energies here, this origin for the increase in σ is not only physically justified, but indeed the only way to account for the similar energetic disorder computed for CC-100 and CA-100. Notably, gliding-type paracrystallinity, measured along the c axis, does not affect the electrostatic interactions between charged conjugated planes.

In addition to the regioregularity effect on energetic disorder, we observe shifts of the mean $\langle E \rangle$ of the site-energy distributions. To explain these, we first emphasize that due to the negative quadrupole moment of thiophene dimers, a hole localized on a polymer chain will be stabilized already on an electrostatic level due to the quadrupole moment of the neighboring chains, even without including polarization.⁷⁷ This means that better geometrical overlap of the backbones leads to a larger stabilization of holes. During the transition from a staggered to a coplanar stacking, the reduction in tilt angle leads to enhanced hole-quadrupole interactions. These are responsible for the lower $\langle E \rangle$ in CA-100 compared to CC-100. For the systems of lower regioregularity, the transition in backbone stacking is less pronounced (see Figure 4b), since side-chain defects already lead to a slight planarization of the backbone, and hence lowered ionization potentials (compare the site-energy mean of CC-90 to CC-100). As the backbone stacking turns entirely coplanar, side-chain defects lead to a high degree of slipping-type paracrystallinity (Figure 7c). This implies a weakening of the energetically favorable hole-quadrupole interaction, and therefore an increase in the mean of the site-energy distribution when comparing CC-90 to CA-90. In addition to this shift of the mean, slipping defects in CA-90 lead to a slight deviation from a Gaussian shape of the DOS, which we can relate to the long tail of distances d_{100} in Figure 7c.

Summing up, we have shown how the external contribution to the energetic density of states is intimately connected with paracrystallinity along the π -stacking direction, with energetic disorder σ linearly related to the amplitude of backbone–backbone distance fluctuations, and the mean of the backbone–backbone distance distribution analogously related to the average site energy $\langle E \rangle$. In section IVC, we will show that this energetic disorder can be treated as *static* on the time scale of an electron-transfer reaction.

B. Electronic Couplings. The distributions of the electronic coupling elements were calculated as described in the Methodology section and are shown in Figure 8b. Unexpectedly, the 100% regioregular P3HT with crystalline side chains (CC-100) has (on average) lower electronic couplings than the corresponding 90% regioregular phase (CC-90). This peculiar effect is most likely due to the different interlevel shift observed for the two regioregularities, see Figure 7. Transfer integrals tend to be very sensitive to this structural mode.⁷⁸ For two perfectly aligned, optimized chains, the coupling element $|J_{ij}|^2$ can vary between 0 and 10^{-2} eV as the backbones are shifted with respect to each other along the

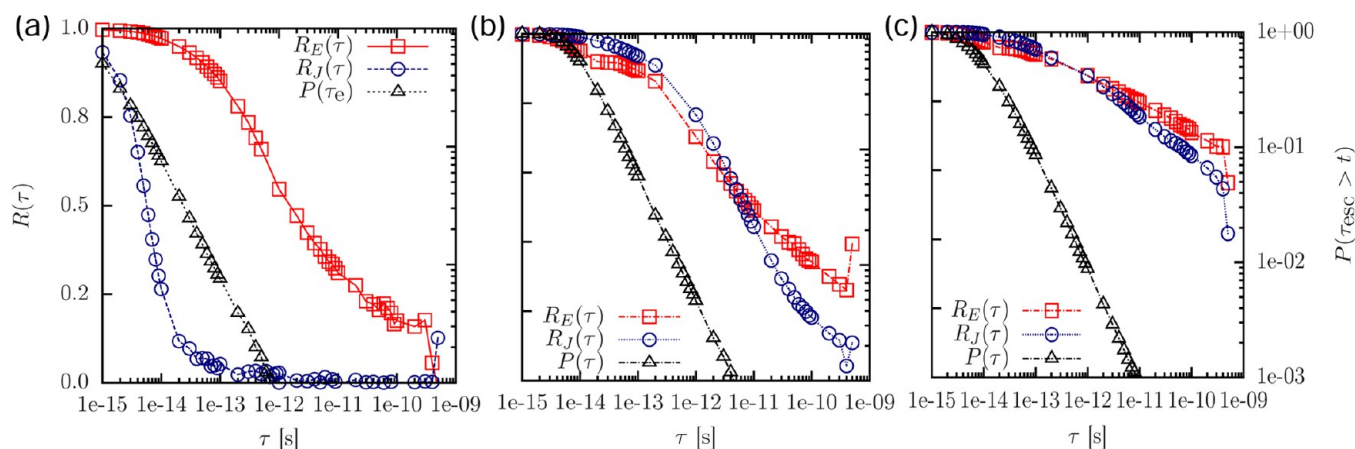


Figure 9. The time scales of transport and transport parameters in material systems of different chemical composition, side-chain order and side-chain density: PBTtT (left), P3HT-100 (center), and P3HT-90 (right) estimated via the time autocorrelation function of transfer integrals (blue circles), site energies (red squares) and the tail distribution of escape times (black triangles). The data in panel a is reproduced from Poelking et al.⁷⁵

polymer's long axis by one repeat unit, thus yielding a \sin^2 -type variation of $|J_{ij}|^2$ with interlevel shift.

Side-chain melting leads to a broadening of the distributions and a tail of very small couplings, down to 10^{-6} eV (even though only nearest neighbors are present in the neighbor list). This would obviously result in rather small average mobility values.⁷⁹ However, this conclusion is valid only if (one-dimensional) charge-carrier transport were to occur within a static snapshot of the system; in reality, both transfer integrals and site energies are time-dependent. In order to understand whether such a static picture can be used in our case, we evaluate the distributions of relaxation times of the electronic coupling elements and site energies and compare them to the distribution of escape times of a charge carrier in section IV C.

C. Autocorrelation Functions. Molecular thermal motion leads to time-dependence of both J_{ij} and E_i . A part of this dependence (fast vibrations of the promoting mode) is already accounted for in eq 1. Relaxation times of slow (and often anharmonic) modes shall be compared to the distribution of inverse charge transfer rates in order to validate the assumed nonadiabaticity of the charge transfer reaction. To explore the limitations associated with simulating charge transfer in a frozen morphology, we compare charge escape times, τ_{esc} to relaxation times of the backbone as reflected both in the electronic coupling elements and site energies.

Charge escape rates are defined as $\omega_{\text{esc}}^{(i)} = \sum_j \omega_{ij}$, where ω_{ij} is the hole-transfer rate from site i to site j , eq 1, and the sum is evaluated for all nearest neighbors j of site i . The escape time, i.e., the average time a charge spends localized on a given site, can then be obtained as $\tau_{\text{esc}}^{(i)} = 1/\omega_{\text{esc}}^{(i)}$. From the resulting distribution of escape times, $p(t)$, we calculate the distribution (exceedence, or complementary cumulative distribution function), $P(\tau) = \int_{\tau}^{\infty} p(t) dt$, which is proportional to the number of sites with an escape time larger than τ .

Backbone dynamics are estimated from the time autocorrelation functions $R_E(\tau)$ for site energies $E^{(i)}$ and $R_J(\tau)$ for transfer amplitudes, $|J_{ij}|^2$,

$$R_E(\tau) = \frac{\langle (E_t^{(i)} - \langle E \rangle)(E_{t+\tau}^{(i)} - \langle E \rangle) \rangle}{\sigma^2} \quad (6)$$

where $\langle \dots \rangle$ denotes the ensemble average; the width σ and average $\langle E \rangle$ have the same meaning as in the electronic density

of states, eq 5. The analogous expression is used for the transfer integrals.

The autocorrelation functions are shown along with the tail distribution of escape times in Figure 8d. Interestingly, the relaxation of the electronic coupling elements and site energies occurs on similar time scales in spite of their dissimilar physical origins: Site energies are related to long-range electrostatic interactions, where averaging occurs over a large number of nearest neighbors and leads to spatial correlations. On the other hand, the electronic coupling elements (to a first approximation) only depend on the geometries of pairs of molecules, which results in increased sensitivity to thermal motions of the internal degrees of freedom. The reason for similar time scales is the chemical structure of P3HT: Every thiophene unit is linked to an alkyl side chain with slow dynamics both in the crystalline and amorphous phase. This overdamps the backbone dynamics, in particular torsional motions of thiophene units, and results in slow variations of electronic couplings.

Interestingly, in a similar conjugated polymer, PBTtT, where a thienothiophene unit is not linked to a side chain (implying a lower side-chain density and better crystallinity), electronic couplings have significantly faster dynamics, which is beneficial for charge transport.⁷⁵ Notably, the high side-chain density in P3HT, where every repeat unit is linked to an alkyl group, overdamps the dynamics of the backbone: Considering Figure 9, one can see how the regime of charge transport changes with respect to transfer integrals from disorder-limited in the case of P3HT to diffusion-limited in the case of PBTtT due to the difference in backbone dynamics that is fostered by the side-chain structure.

Comparing the 100% and 90% regioregular materials, we note how the defects in side-chain attachment lead to slower dynamics, with decorrelation times significantly increased over the defect-free case. More quantitatively, on intermediate delay times on the range of tenth of picoseconds, the time evolution is in all cases governed by a logarithmic diffusion-driven decorrelation of both site energies and electronic couplings. Regarding site energies, the dimensionless exponent that characterizes this decorrelation for CA-100 assumes a value three times larger than for CA-90. This again highlights how defects in regioregularity induce glass-like features in structure and dynamics. Analyzing the decorrelation in polymorphs I' and I, this exponent remains the same. However, there is an

offset between the two time characteristics that persists up to delay times in the nanosecond range. This offset is a consequence of structural decorrelations within the first few femtoseconds: Side chains in form I are in a more disordered state, and hence more effectively damp backbone dynamics as compared to hexyl groups in form I', which apparently dominates dynamics on this short time scale.

The time evolution of site energies and electronic couplings should be compared to the tail distribution of escape times, $P(\tau)$. On a log–log scale, the linear shape for large τ implies a power-law decay $P(\tau) \sim O(1/\tau)$. Hence, reducing the tail distribution to just one time scale to be compared to τ_E or τ_I is not possible (the majority of sites has an escape time far smaller than any relaxation time, but it is the sites in the tail of the exceedence that act as shallow or deep traps and significantly slow down transport). Yet, in the systems at hand, even the slowest escape times for holes do not extend into the decorrelation regime ($\tau \sim \text{ns}$) insinuated by $R_E(\tau)$ and $R_I(\tau)$. We therefore conclude that charge-carrier dynamics is in practice limited by the *static* disorder of electronic couplings and site energies, since their relaxation times exceed typical time scales of hopping transport in the system. Hence, it is possible to resort to a single charge-transfer rate to describe transport, eq 1, without time-averaging of electronic couplings of a pair of molecules, as it was needed in columnar discotic liquid crystals⁸⁰ or PBTTT.⁷⁵ On the aside, we note that it is also possible to accurately account for the explicit time-dependence of electronic couplings by employing semiclassical dynamics.^{81–83}

D. Charge Mobility. Since the transport has a one-dimensional character, it can already be anticipated that a broad and *static* distribution of electronic couplings (see section IVB and section IVB) limits charge mobility along lamellae.^{67,79,84–88} Indeed, Figure 8c shows that mobility values, evaluated for 5000 lamellae, each consisting of 40 stacked chains, are broadly distributed, with small mobilities as low as $10^{-7} \text{cm}^2/(\text{V s})$. Yet, by comparing the four materials, we find that the associated mobility distributions are fundamentally different from what one would expect solely on the grounds of electronic couplings, Figure 8b. From previous sections we recall that the distribution of transfer integrals is determined by the polymorph at hand (I' or I) and not sensitive to a small decrease in regioregularity, whereas energetic disorder is governed by regioregularity defects and as such polymorph-independent. Aiming for high mobilities, one should hence prefer high regioregularity over medium regioregularity due to the smaller energetic disorder and P3HT form I' over P3HT form I due to higher electronic couplings. The mobility implicitly depends on both quantities and as such mirrors a clear trend, with the average mobility decreasing from CC-100 to CA-100 to CC-90 to CA-90. These averages are indicated by vertical bars in Figure 8b and summarized in Table 1.

In the case of 100% regioregular P3HT, we can compare these values to mobilities extracted from experimental transistor

I–V curves on P3HT nanofibers.^{32,73,74} Note that a comparison to mobilities obtained from time-of-flight experiments is problematic due to the existence of grain boundaries, which impede transport. We find that our simulated mobilities are in excellent agreement with field-effect mobilities in P3HT nanofibers (devoid of these grain boundaries), with the gray bar in Figure 4c indicating the range of experimental values ($\mu = 0.01\text{--}0.06 \text{cm}^2/(\text{V s})$) obtained for different solvent and processing conditions. Note that in general, the mobility depends strongly on the charge-carrier concentration. We expect this dependence to be mitigated here due to the small energetic disorder combined with the low-dimensional character of the transport, as is also indicated by the good agreement with experiment achieved in a previous computational study.⁷⁵

Note that the effect of regioregularity on charge transport has been studied experimentally in the context of time-of-flight experiments,¹² where a reduction in regioregularity by 5% led to a decrease in mobility by a factor five. In our simulations, we were dealing with a reduction in regioregularity by 10%, comparing systems CA-100 and CA-90 (i.e., form-I P3HT, as most likely studied in the aforementioned experiment), translates into a factor 10 decrease in mobility, from $\langle \mu \rangle = 0.0231 \text{cm}^2/(\text{V s})$ down to $0.0029 \text{cm}^2/(\text{V s})$. This indicates that the decrease in mobility is due to intradomain instead of interdomain transport. According to our results, the regioregularity effect is exclusively due to enhanced energetic disorder. Combining these findings with a simulation study that considered the intramolecular contribution to the density of states,³⁵ we can summarize that the intramolecular contribution to the DOS shape and trap density are little affected by the presence of regioregularity defects. The higher mobility in the regioregular material is entirely attributable to a narrowing of the density of states that results from increased order in hole–quadrupole interaction distances.

The effect of energetic disorder is further amplified in the case of P3HT due to the one-dimensional character of transport, since a single energetic trap can impede transport through the entire lamella.⁷⁹ This effect is visualized in Figure 10a–d, where the energetic landscape is exemplified for three lamellae at five different simulation times and four materials. Here, the widths of the bonds connecting the hopping sites are proportional to the logarithm of squared electronic coupling elements, while the heights of the vertical bars are proportional to the occupation probability of a specific site. The gray scale indicates the average mobility of a particular lamella, with darker colors corresponding to lower mobilities.

One can see that site-energy profiles are highly corrugated and spatially correlated, with weaker correlations in the case of reduced regioregularity. Note also that deep energetic traps found in CC-90 and CA-90 persist throughout the entire time range shown here, as expected based on the associated time autocorrelation functions. Studying the landscape-mobility correlation more closely, it becomes apparent that transport in CC-100 and CA-100 is strongly dominated by weak links (small transfer integrals) that adversely affect the lamellar mobility, whereas transport in CC-90 and CA-90 suffers mostly from energetic disorder, as already suspected based on the shape of the mobility distribution in Figure 8d. It might also happen that, for larger widths of the energetic disorder, the limiting factor for hole transfer will be the dynamics of energetic traps existing in the system due to thermal fluctuations of the molecular structure.

Table 1. Simulated Mobilities Obtained for P3HT Crystals of Different Structure and Regioregularity for Transport along the Lamellar Axis with an External Electric Field of 10^4V/m Applied in the Transport (π -Stacking) Direction

system	CC-100	CA-100	CC-90	CA-90
$\langle \mu \rangle [\text{cm}^2/(\text{V s})]$	0.0468	0.0231	0.0090	0.0029

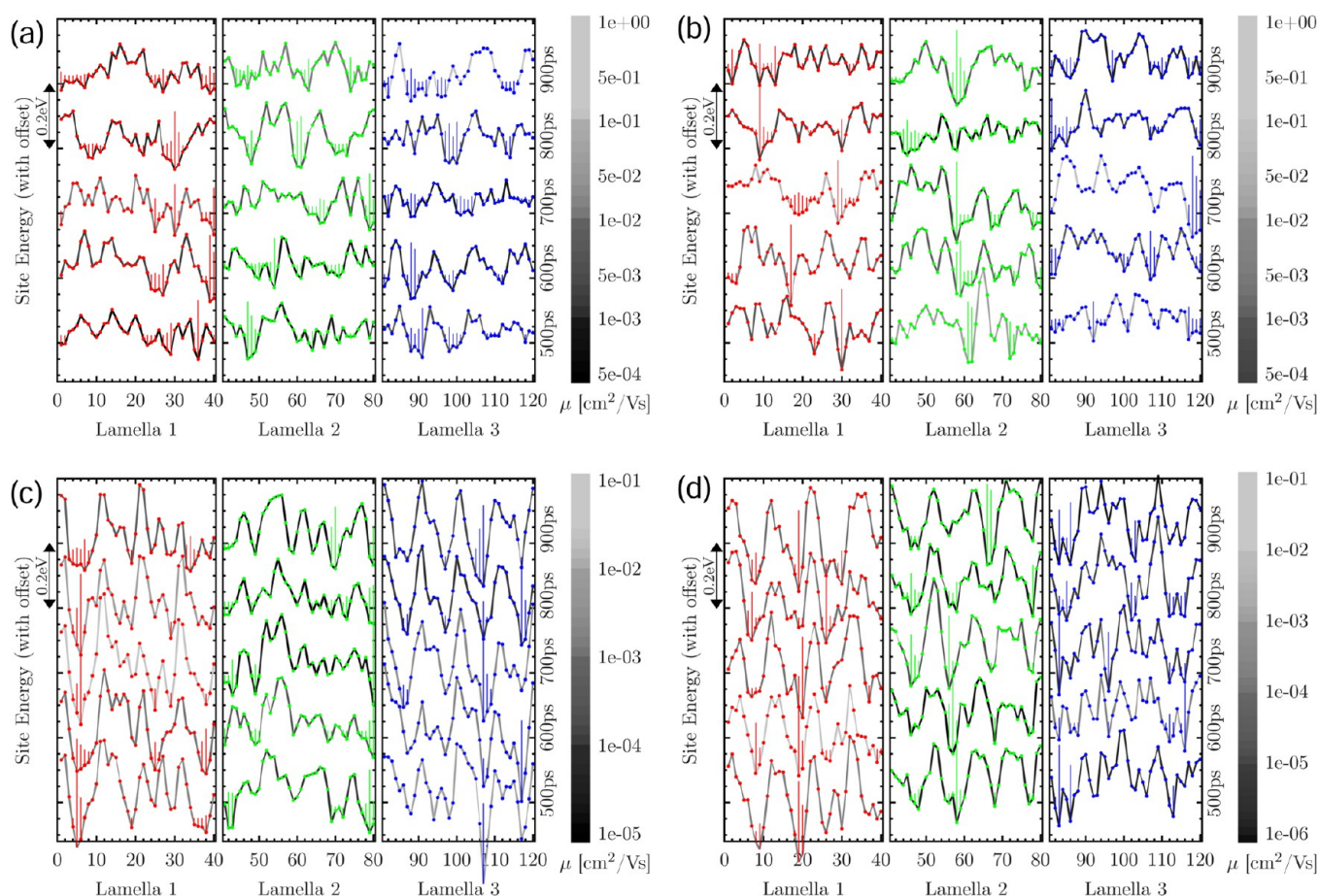


Figure 10. Offset energetic landscapes for (a) CC-100, (b) CA-100, (c) CC-90, and (d) CA-90 exemplified for three lamellae and five time frames. Widths of connecting lines between neighboring sites are proportional to the logarithm of squared electronic couplings. The length of vertical colored lines indicates the occupation probability of the site. The lamellar mobility is coded according to the gray scale to the left. Note the different mobility range for the four systems.

V. CONCLUSIONS

We have investigated structure-mobility relationships in lamellar crystals of P3HT, focusing on the effect of structural transitions in side-chain and backbone packing, defects in regioregularity, dynamic and paracrystalline order.

Apart from the onset of the backbone melting transition at high temperatures (~ 450 K), molecular dynamics performed on large P3HT supercells produced a low-temperature (~ 350 – 375 K) phase transition. In all polymorphs, this transition involves side-chain melting, either from their very crystalline state in form I' or a partially crystalline state in form I into a more disordered (practically amorphous) state. Additionally, in form I', side chain melting is accompanied by the conversion between distinct P3HT polymorphs: The educt (form I') has a tilted backbone configuration, whereas the product (form I) adopts a coplanar, face-on, backbone arrangement. By comparing to experimental studies employing solid-state NMR, X-ray and electron diffraction, as well as infrared spectroscopy, we have obtained a consistent picture of the polymorphic phase behavior of P3HT, with molecular dynamics simulations revealing structural models for the noninterdigitated metastable form I' and thermodynamically stable form I based on a refined force field.

We pinpoint the effect of small concentrations of defects in regioregularity on charge transport properties to reside in the strong intermolecular contribution to the broadening of the

density of states (energetic disorder). The factor-of-10 decrease in simulated mobilities of 90% regioregular materials compared to 100% regioregular systems is exclusively due to the more corrugated *static* (on the time scale of charge transfer) energetic landscape. From the point of view of structure, this in turn could be linked to increased paracrystallinity along the π -stacking direction. We found paracrystallinity parameters to most appropriately reflect the reduction in regioregularity, with slipping-type paracrystallinity responsible for slight deviations from a Gaussian-shaped density of states. Even for the highly regioregular systems, energetic disorder, though small compared to typical amorphous organic semiconductors, has a critical effect on transport due to the one-dimensional charge transport network.

Simulated mobilities are in excellent agreement with experimental field-effect mobilities extracted from measurements on individual P3HT nanofibers. Considering the good agreement with experimental mobilities obtained also for a different polymeric semiconductor (PBTTT),⁷⁵ while employing the same combination of methods, we find the approach to be suited for the quantitative characterization of charge transport in the crystalline lamellar domains that are characteristic of this large class of semiconducting polymers.

■ ASSOCIATED CONTENT

■ Supporting Information

Atomistic molecular-dynamics simulations, force-field parameters, details of charge transport simulations, GROMACS topology, and force-field files for a P3HT chain. This material is available free of charge via the Internet at <http://pubs.acs.org>.

■ AUTHOR INFORMATION

Corresponding Authors

*E-mail: (C.P.) carl.poelking@mpip-mainz.mpg.de.

*E-mail: (D.A.) denis.andrienko@mpip-mainz.mpg.de.

Notes

The authors declare no competing financial interest.

■ ACKNOWLEDGMENTS

This work was partly supported by DFG Program IRTG 1328, DFG Grant SPP 1355, and BMBF Grants MESOMERIE and MEDOS. We are grateful to Kurt Kremer and Mara Jochum for critical reading of the manuscript.

■ REFERENCES

- (1) McCullough, R. D. *Adv. Mater.* **1998**, *10* (2), 93–116.
- (2) McCullough, R. D.; Lowe, R. D. *Chem. Commun.* **1992**, No. 1, 70.
- (3) Meyer, V. *Ber. Dtsch. Chem. Ges.* **1883**, *16* (1), 1465–1478.
- (4) Yamamoto, T.; Sanechika, K.; Yamamoto, A. *J. Polym. Sci., Polym. Lett. Ed.* **1980**, *18* (1), 9–12.
- (5) Lin, J. W.-P.; Dudek, L. P. *J. Polym. Sci., Polym. Chem. Ed.* **1980**, *18* (9), 2869–2873.
- (6) Elsenbaumer, R.; Jen, K.; Oboodi, R. *Synth. Met.* **1986**, *15* (2–3), 169–174.
- (7) Tsumura, A.; Koezuka, H.; Ando, T. *Appl. Phys. Lett.* **1986**, *49* (18), 1210.
- (8) Bao, Z.; Dodabalapur, A.; Lovinger, A. J. *Appl. Phys. Lett.* **1996**, *69* (26), 4108.
- (9) Heeger, A. *Rev. Mod. Phys.* **2001**, *73* (3), 681–700.
- (10) Li, G.; Shrotriya, V.; Huang, J.; Yao, Y.; Moriarty, T.; Emery, K.; Yang, Y. *Nat. Mater.* **2005**, *4* (11), 864–868.
- (11) McCullough, R. D.; Tristram-Nagle, S.; Williams, S. P.; Lowe, R. D.; Jayaraman, M. *J. Am. Chem. Soc.* **1993**, *115* (11), 4910–4911.
- (12) Mauer, R.; Kastler, M.; Laquai, F. *Adv. Funct. Mater.* **2010**, *20* (13), 2085–2092.
- (13) Crossland, E. J. W.; Tremel, K.; Fischer, F.; Rahimi, K.; Reiter, G.; Steiner, U.; Ludwigs, S. *Adv. Mater.* **2012**, *24* (6), 839–844.
- (14) Prosa, T. J.; Winokur, M. J.; McCullough, R. D. *Macromolecules* **1996**, *29* (10), 3654–3656.
- (15) Zen, A.; Paum, J.; Hirschmann, S.; Zhuang, W.; Jaiser, F.; Asawapirom, U.; Rabe, J. P.; Scherf, U.; Neher, D. *Adv. Funct. Mater.* **2004**, *14* (8), 757–764.
- (16) Kline, R. J.; McGehee, M. D.; Kadnikova, E. N.; Liu, J.; Fréchet, J. M. J.; Toney, M. F. *Macromolecules* **2005**, *38* (8), 3312–3319.
- (17) Ballantyne, A. M.; Chen, L.; Dane, J.; Hammant, T.; Braun, F. M.; Heeney, M.; Duffy, W.; McCulloch, I.; Bradley, D. D. C.; Nelson, J. *Adv. Funct. Mater.* **2008**, *18* (16), 2373–2380.
- (18) Kohn, P.; Huettner, S.; Komber, H.; Senkovskyy, V.; Tkachov, R.; Kiriy, A.; Friend, R. H.; Steiner, U.; Huck, W. T. S.; Sommer, J.-U.; Sommer, M. *J. Am. Chem. Soc.* **2012**, *134* (10), 4790–4805.
- (19) Pascui, O. F.; Lohwasser, R.; Sommer, M.; Thelakkat, M.; Thurm-Albrecht, T.; Saalwächter, K. *Macromolecules* **2010**, *43* (22), 9401–9410.
- (20) Brinkmann, M. *J. Polym. Sci., Part B: Polym. Phys.* **2011**, *49* (17), 1218–1233.
- (21) Yuan, Y.; Zhang, J.; Sun, J.; Hu, J.; Zhang, T.; Duan, Y. *Macromolecules* **2011**, *44* (23), 9341–9350.
- (22) Abdou, M. S. A.; Orfino, F. P.; Son, Y.; Holdcroft, S. *J. Am. Chem. Soc.* **1997**, *119* (19), 4518–4524.
- (23) McCulloch, I.; Heeney, M.; Chabinyc, M. L.; De-Longchamp, D.; Kline, R. J.; Coelle, M.; Duffy, W.; Fischer, D.; Gundlach, D.; Hamadani, B.; Hamilton, R.; Richter, L.; Salleo, A.; Shkunov, M.; Sparrowe, D.; Tierney, S.; Zhang, W. *Adv. Mater.* **2009**, *21* (10–11), 1091–1109.
- (24) Liversedge, I. A.; Higgins, S. J.; Giles, M.; Heeney, M.; McCulloch, I. *Tetrahedron Lett.* **2006**, *47* (29), 5143–5146.
- (25) Ma, C.-Q.; Mena-Osteritz, E.; Debaerdemaeker, T.; Wienk, M. M.; Janssen, R. A. J.; Bäuerle, P. *Angew. Chem., Int. Ed.* **2007**, *46* (10), 1679–1683.
- (26) Richter, T. V.; Link, S.; Hanselmann, R.; Ludwigs, S. *Macromol. Rapid Commun.* **2009**, *30* (15), 1323–1327.
- (27) Link, S.; Richter, T.; Yurchenko, O.; Heinze, J.; Ludwigs, S. *J. Phys. Chem. B* **2010**, *114* (33), 10703–10708.
- (28) McCulloch, I.; Heeney, M.; Bailey, C.; Genevicius, K.; MacDonald, I.; Shkunov, M.; Sparrowe, D.; Tierney, S.; Wagner, R.; Zhang, W.; Chabinyc, M. L.; Kline, R. J.; McGehee, M. D.; Toney, M. F. *Nat. Mater.* **2006**, *5* (4), 328–333.
- (29) van Mullekom, H.; Vekemans, J.; Havinga, E.; Meijer, E. *Mater. Sci. Eng. R Rep.* **2001**, *32* (1), 1–40.
- (30) Crossland, E. J. W.; Rahimi, K.; Reiter, G.; Steiner, U.; Ludwigs, S. *Adv. Funct. Mater.* **2011**, *21* (3), 518–524.
- (31) Merlo, J. A.; Frisbie, C. D. *J. Polym. Sci., Part B: Polym. Phys.* **2003**, *41* (21), 2674–2680.
- (32) Bolsée, J.-C.; Oosterbaan, W. D.; Lutsen, L.; Vanderzande, D.; Manca, J. *Org. Electron.* **2011**, *12* (12), 2084–2089.
- (33) Niles, E. T.; Roehling, J. D.; Yamagata, H.; Wise, A. J.; Spano, F. C.; Moulé, A. J.; Grey, J. K. *J. Phys. Chem. Lett.* **2012**, *3* (2), 259–263.
- (34) Dag, S.; Wang, L.-W. *J. Phys. Chem. B* **2010**, *114* (18), 5997–6000.
- (35) McMahan, D. P.; Cheung, D. L.; Goris, L.; Dacuna, J.; Salleo, A.; Troisi, A. *J. Phys. Chem. C* **2011**, *115* (39), 19386–19393.
- (36) Alexiadis, O.; Mavrantzas, V. G. *Macromolecules* **2013**, *46* (6), 2450–2467.
- (37) Moreno, M.; Casalegno, M.; Raos, G.; Meille, S. V.; Po, R. *J. Phys. Chem. B* **2010**, *114* (4), 1591–1602.
- (38) Gus'kova, O. A.; Khalatur, P. G.; Khokhlov, A. R. *Macromol. Theory Simul.* **2009**, *18* (4–5), 219–246.
- (39) Huang, D. M.; Faller, R.; Do, K.; Moulé, A. J. *J. Chem. Theory. Comput.* **2010**, *6* (2), 526–537.
- (40) Lee, C.-K.; Pao, C.-W.; Chu, C.-W. *Energy Environ. Sci.* **2011**, *4* (10), 4124–4132.
- (41) Gemünden, P.; Poelking, C.; Kremer, K.; Andrienko, D.; Daoulas, K. C. *Macromolecules* **2013**, *46* (14), 5762–5774.
- (42) Vukmirovic, N.; Wang, L.-W. *J. Phys. Chem. B* **2011**, *115* (8), 1792–1797.
- (43) Jorgensen, W. L.; Tirado-Rives, J. *J. Am. Chem. Soc.* **1988**, *110* (6), 1657–1666.
- (44) Jorgensen, W. L.; Tirado-Rives, J. *J. Comput. Chem.* **2005**, *26* (16), 1689–1700.
- (45) Berendsen, H. J. C.; Postma, J. P. M.; van Gunsteren, W. F.; DiNola, A.; Haak, J. R. *J. Chem. Phys.* **1984**, *81* (8), 3684.
- (46) Bussi, G.; Donadio, D.; Parrinello, M. *J. Chem. Phys.* **2007**, *126* (1), 014101.
- (47) Hess, B.; Kutzner, C.; van der Spoel, D.; Lindahl, E. *J. Chem. Theory Comput.* **2008**, *4* (3), 435–447.
- (48) May, V.; Kühn, O. *Charge and Energy Transfer Dynamics in Molecular Systems*, 3rd, revised and enlarged ed.; Wiley-VCH: New York, 2011.
- (49) Brédas, J. L.; Calbert, J. P.; Filho, D. A. d. S.; Cornil, J. *Proc. Natl. Acad. Sci. U.S.A.* **2002**, *99* (9), 5804–5809.
- (50) Coropceanu, V.; Cornil, J.; da Silva Filho, D. A.; Olivier, Y.; Silbey, R.; Brédas, J.-L. *Chem. Rev.* **2007**, *107* (4), 926–952.
- (51) Kirkpatrick, J. *Int. J. Quantum Chem.* **2008**, *108* (1), 51–56.
- (52) Marcus, R. A. *Rev. Mod. Phys.* **1993**, *65* (3), 599.
- (53) Baumeier, B.; Kirkpatrick, J.; Andrienko, D. *Phys. Chem. Chem. Phys.* **2010**, *12* (36), 11103.
- (54) Baumeier, B.; May, F.; Lennartz, C.; Andrienko, D. *J. Mater. Chem.* **2012**, *22* (22), 10971.

- (55) Rühle, V.; Lukyanov, A.; May, F.; Schrader, M.; Vehoff, T.; Kirkpatrick, J.; Baumeier, B.; Andrienko, D. *J. Chem. Theory Comput.* **2011**, *7* (10), 3335–3345.
- (56) Thole, B. *Chem. Phys.* **1981**, *59* (3), 341–350.
- (57) Prosa, T. J.; Winokur, M. J.; Moulton, J.; Smith, P.; Heeger, A. J. *Macromolecules* **1992**, *25* (17), 4364–4372.
- (58) Wu, Z.; Petzold, A.; Henze, T.; Thurn-Albrecht, T.; Lohwasser, R. H.; Sommer, M.; Thelakkat, M. *Macromolecules* **2010**, *43* (10), 4646–4653.
- (59) Kayunkid, N.; Uttiya, S.; Brinkmann, M. *Macromolecules* **2010**, *43* (11), 4961–4967.
- (60) Maillard, A.; Rochefort, A. *Phys. Rev. B* **2009**, *79* (11), 115207.
- (61) Rahimi, K.; Botiz, I.; Stingelin, N.; Kayunkid, N.; Sommer, M.; Koch, F. P. V.; Nguyen, H.; Coulembier, O.; Dubois, P.; Brinkmann, M.; Reiter, G. *Angew. Chem., Int. Ed.* **2012**, *51* (44), 11131–11135.
- (62) Dudenko, D.; Kiersnowski, A.; Shu, J.; Pisula, W.; Sebastiani, D.; Spiess, H. W.; Hansen, M. R. *Angew. Chem., Int. Ed.* **2012**, *51* (44), 11068–11072.
- (63) Liu, J.; Sun, Y.; Gao, X.; Xing, R.; Zheng, L.; Wu, S.; Geng, Y.; Han, Y. *Langmuir* **2011**, *27* (7), 4212–4219.
- (64) Marcon, V.; Breiby, D. W.; Pisula, W.; Dahl, J.; Kirkpatrick, J.; Patwardhan, S.; Grozema, F.; Andrienko, D. *J. Am. Chem. Soc.* **2009**, *131* (32), 11426–11432.
- (65) Hansen, M. R.; Graf, R.; Sekharan, S.; Sebastiani, D. *J. Am. Chem. Soc.* **2009**, *131* (14), 5251–5256.
- (66) Hansen, M. R.; Schnitzler, T.; Pisula, W.; Graf, R.; Müllen, K.; Spiess, H. W. *Angew. Chem., Int. Ed.* **2009**, *48* (25), 4621–4624.
- (67) May, F.; Marcon, V.; Hansen, M. R.; Grozema, F.; Andrienko, D. *J. Mater. Chem.* **2011**, *21* (26), 9538.
- (68) Hsu, W. P.; Levon, K.; Ho, K. S.; Myerson, A. S.; Kwei, T. K. *Macromolecules* **1993**, *26* (6), 1318–1323.
- (69) Pankaj, S.; Beiner, M. *Soft Matter* **2010**, *6* (15), 3506.
- (70) Marcon, V.; Vehoff, T.; Kirkpatrick, J.; Jeong, C.; Yoon, D. Y.; Kremer, K.; Andrienko, D. *J. Chem. Phys.* **2008**, *129* (9), 094505.
- (71) Rivnay, J.; Noriega, R.; Northrup, J. E.; Kline, R. J.; Toney, M. F.; Salleo, A. *Phys. Rev. B* **2011**, *83* (12), 121306.
- (72) DeLongchamp, D. M.; Kline, R. J.; Jung, Y.; Lin, E. K.; Fischer, D. A.; Gundlach, D. J.; Cotts, S. K.; Moad, A. J.; Richter, L. J.; Toney, M. F.; Heeney, M.; McCulloch, I. *Macromolecules* **2008**, *41* (15), 5709–5715.
- (73) Shimomura, T.; Takahashi, T.; Ichimura, Y.; Nakagawa, S.; Noguchi, K.; Heike, S.; Hashizume, T. *Phys. Rev. B* **2011**, *83* (11), 115314.
- (74) Mas-Torrent, M.; Boer, D. d.; Durkut, M.; Hadley, P.; Schenning, A. P. H. J. *Nanotechnology* **2004**, *15* (4), S265–S269.
- (75) Poelking, C.; Ivanov, V.; Kremer, K.; Risko, C.; Brédas, J.-L.; Andrienko, D.; Eunkyung, C. *J. Phys. Chem. C* **2013**, *117* (4), 1633–1640.
- (76) Baessler, H. *Phys. Status Solidi B* **1993**, *175* (1), 15–56.
- (77) D'Avino, G.; Mothy, S.; Muccioli, L.; Zannoni, C.; Wang, L.; Cornil, J.; Beljonne, D.; Castet, F. *J. Phys. Chem. C* **2013**, *117* (25), 12981–12990.
- (78) Fogel, Y.; Zhi, L.; Rouhanipour, A.; Andrienko, D.; Räder, H. J.; Müllen, K. *Macromolecules* **2009**, *42* (18), 6878–6884.
- (79) Scher, H.; Alexander, S.; Montroll, E. W. *Proc. Natl. Acad. Sci. U.S.A.* **1980**, *77* (7), 3758–3762.
- (80) Olivier, Y.; Muccioli, L.; Lemaire, V.; Geerts, Y. H.; Zannoni, C.; Cornil, J. *J. Phys. Chem. B* **2009**, *113* (43), 14102–14111.
- (81) Troisi, A.; Cheung, D. L.; Andrienko, D. *Phys. Rev. Lett.* **2009**, *102* (11), 116602.
- (82) Vehoff, T.; Chung, Y. S.; Johnston, K.; Troisi, A.; Yoon, D. Y.; Andrienko, D. *J. Phys. Chem. C* **2010**, *114* (23), 10592–10597.
- (83) Vehoff, T.; Baumeier, B.; Troisi, A.; Andrienko, D. *J. Am. Chem. Soc.* **2010**, *132* (33), 11702–11708.
- (84) Kirkpatrick, J.; Marcon, V.; Nelson, J.; Kremer, K.; Andrienko, D. *Phys. Rev. Lett.* **2007**, *98* (22), 227402.
- (85) Marcon, V.; Kirkpatrick, J.; Pisula, W.; Andrienko, D. *Phys. Status Solidi B* **2008**, *245* (5), 820–824.
- (86) Andrienko, D.; Kirkpatrick, J.; Marcon, V.; Nelson, J.; Kremer, K. *Phys. Status Solidi B* **2008**, *245* (5), 830–834.
- (87) Schrader, M.; Fitzner, R.; Hein, M.; Elschner, C.; Baumeier, B.; Leo, K.; Riede, M.; Bäuerle, P.; Andrienko, D. *J. Am. Chem. Soc.* **2012**, *134* (13), 6052–6056.
- (88) Schrader, M.; Körner, C.; Elschner, C.; Andrienko, D. *J. Mater. Chem.* **2012**, *22* (41), 22258–22264.